NJC

Check for updates

Structure–redox reactivity relationships in Co₁₋ₓZnₓFe₂O₄: the role of stoichiometry

Tetiana Tatarchuk, [ID] *[ab] Natalia Paliychuk,[b] Michał Pacia,[c] Wojciech Kaspera,[c] Wojciech Macyk, [ID][c] Andrzej Kotarba, [ID][c] Bogdan F. Bogacz, [ID][d] Antoni T. Pędziwiatr, [ID][d] Ivan Mironyuk,[a] Renata Gargula,[d] Piotr Kurzydło [ID][d] and Alexander Shyichuk [ID][e]

Nanostructured Zn-doped cobalt ferrites (Co₁₋ₓZnₓFe₂O₄, where x ranges from 0.0 to 1.0 with a step of 0.1) were studied in order to elucidate the relation between their cationic distribution within the spinel sublattices and catalytic properties. The thermal transformation of the precursors (metal hydroxides) obtained through the hydroxide co-precipitation method was studied by DTA, TGA and FTIR. The thermal behavior of the precursors showed that cobalt ferrite was formed at a lower temperature (376 °C) in comparison to zinc ferrite (478 °C). FTIR analysis revealed vibrational bands around 400 cm⁻¹ and 600 cm⁻¹ related to $(MO_4)^{6-}$ and $(MO_6)^{9-}$ groups, respectively. The cationic distribution was determined from Mössbauer spectra analysis and the results showed that Zn ions occupy the A-sites, while Co and Fe ions are located in the A- and B-sites. The spectra indicate spinel magnetic ordering in samples with x = 0.0...0.5. The increase in Zn content influences the difference in the Pauling electronegativities, distances between magnetic ions (hopping length) and polaron radius of Co₁₋ₓZnₓFe₂O₄ ferrites, inducing changes in the ionic bond strength for the A- and B-sites. Photoelectrochemical measurements demonstrated that the introduction of Zn^{2+} into the spinel structure modifies the ability of the materials to reduce O₂. Whereas photoinduced reduction of dioxygen at CoFe₂O₄ competes successfully with anodic photocurrent generation (observed as a decrease of photocurrent), for ZnFe₂O₄ this process is negligible. The relation between the cationic distribution (analyzed in terms of anti-structure modeling) and the catalytic activity of spinel ferrites was demonstrated for the example of the soot combustion process. It was shown that the octahedral cobalt centers exhibit a higher catalytic activity than the tetrahedral ones.

1. Introduction

Nowadays, spinel compounds have attracted attention among scientists due to their unique properties and wide applications in different fields. Spinel ferrites exhibit required properties like chemical stability, magnetism and superparamagnetism, high catalytic and photocatalytic activity *etc.* The spinel structure exhibits face centered close packing with divalent and trivalent metal cations in the tetrahedral (A) and octahedral [B] positions.[1,2]

[a] *Department of Chemistry, Vasyl Stefanyk Precarpathian National University, Ivano-Frankivsk, 76018, Ukraine. E-mail: tatarchuk.tetyana@gmail.com*

[b] *Educational and Scientific Center of Material Science and Nanotechnology, Vasyl Stefanyk Precarpathian National University, Ivano-Frankivsk, 76018, Ukraine*

[c] *Faculty of Chemistry, Jagiellonian University, ul. Gronostajowa 2, 30-387 Kraków, Poland*

[d] *M. Smoluchowski Institute of Physics, Jagiellonian University, ul. Łojasiewicza 11, 30-348 Kraków, Poland*

[e] *Faculty of Chemical Technology and Engineering, UTP University of Science and Technology, 3, Seminaryjna str., 85-326, Bydgoszcz, Poland*

Both the physico-chemical properties of the spinel ferrites and particle sizes crucially depend on the distribution of cations among the octahedral and tetrahedral sites of the spinel structure and can be changed by controlled cation substitution achieved in practice using different synthesis methods such as co-precipitation,[3] hydrothermal treatment,[4] synthesis in microemulsions,[5] the solution combustion method,[6] microwave combustion synthesis,[7,8] the sol–gel method,[9–11] *etc.* Among these methods, the co-precipitation technique has many advantages such as the possibility to obtain nanostructural materials with good homogeneity, reproducibility and desired morphology.

A large number of studies have reported different spinel properties as a function of possible cation substitutions. In addition, magnetic spinels could be very good candidates for magnetic cores in drug delivery and for magnetic carriers in sorption and catalysis for environmental processes due to their easy separation from aqueous or gaseous media. Cunha *et al.*[12] reported that the spinel structured iron oxides MFe₂O₄ (M = Cu²⁺ and Co²⁺), magnetite (Fe₃O₄) and maghemite (γ-Fe₂O₃)

were investigated as catalysts for sulfide oxidation in aqueous medium. In the presence of Co the catalytic activity towards oxidation of sulfide to polysulfides increased substiantialy. S. Mobini et al.[13] have synthesized a $CuCr_2O_4$ spinel catalyst by the surfactant-assisted hydrothermal technique and investigated its potential application in the CO oxidation process. The Cr-containing spinels $MgCr_2O_4$ and $CoCr_2O_4$, prepared via the sol–gel method, were investigated as catalysts for catalytic combustion of methane by J. Hu et al.[14] A. M. Banerjee et al.[15] investigated $CoFe_2O_4$, $NiFe_2O_4$ and $CuFe_2O_4$ ferrospinels as catalysts for sulfuric acid decomposition. The relation between the sulfate decomposition rate and the electronegativity of metal cations in the spinel sublattice was demonstrated.

However, there are no reports comparing the structural and spectroelectrochemical properties of ferrospinels with their catalytic activity, in particular in the soot combustion process. Particulate matter is one of the most harmful parts of pollution emitted from diesel engines.[16] It consists mostly of soot, which can be described as a mixture of amorphous carbon and a variety of organic pollutants, some of which possess cancero- and mutagenic properties. Due to the nanometric particle size soot is very volatile and easily penetrates through the skin and lungs. Continuously increasing use of both mobile and stationary diesel engines results in new emission regulations established by the European Commission every few years with EURO6 being the most recent one. The most effective solution for reduction of soot particle emission from diesel engines is a catalytic diesel particulate filter (cDPF). The walls of the filter are covered with catalysts that lower the temperature of soot oxidation ignition so it can be removed in the diesel exhaust conditions. Catalysts used commercially are based on noble metals (Pt, Pd), which results in a high price of the cDPF systems, therefore creating the demand for an alternative that is much cheaper while exhibiting high catalytic activity. The most promising materials in terms of these criteria are based on transition metal oxides. The most intensively investigated one is ceria.[17] Special attention has been paid lately towards transition metal oxides (mainly Fe, Mn, Co, Cr and Cu), including perovskites[18] and spinels.[19–21] Among spinels, cobalt based materials exhibit extraordinary catalytic activity.[19,21] Although cobalt is significantly more expensive than iron, manganese or zinc, mixed transition metal oxides may provide an attractive alternative to noble metal based systems used commercially. Thus, mixed spinels are being synthesized and investigated in terms of activity in soot oxidation in order to design materials that would be of a lower price and promising catalytic performance.

This study demonstrates for the first time a strong relation between the cationic distribution and spectroelectrochemical and catalytic properties of Co–Zn ferrite nanoparticles. A new approach, antistructure modeling, was for the first time proposed for identification of the catalytically active centers in the redox reaction (soot combustion).

Thus, the aim of this work is to systematically investigate the effect of zinc substitution in the lattice of cobalt ferrites on the structural, optical, and catalytic properties of $Co_{1-x}Zn_xFe_2O_4$

$(0.0 \leq x \leq 1.0)$ nanoparticles obtained by the co-precipitation method using Mössbauer spectroscopy, spectroelectrochemical measurements and investigation of their catalytic activity in the soot combustion reaction. A literature survey reveals that catalytic studies of such mixed spinels have not been reported in the context of soot combustion so far. In this paper we address the question of which cations (tetrahedrally or octahedrally coordinated) are responsible for the catalytic activity. A new antistructure modeling approach is proposed as a tool allowing us to resolve this issue.

2. Experimental

2.1. Characterization techniques

A series of cobalt–zinc ferrite samples $Co_{1-x}Zn_xFe_2O_4$ have been synthesized by the chemical co-precipitation method as was described elsewhere.[22] Thermogravimetry (TG) and differential thermal analysis (DTA) of samples (sample weight $\sim$ 400 mg) were carried out in air in a temperature range of 20–1000 °C using a Q1500D Paulik–Paulik–Erdey derivatograph. The heating rate was fixed at 5 °C min^{-1}. α-Al_2O_3 was used as a reference material in this technique. Phase transformations taking place in the sample during heating are recorded. Fourier transform infrared spectra (FT-IR) were recorded in the range of 4000–350 cm^{-1} using an Alpha-P FTIR spectrometer (Bruker) in ATR mode on a diamond window with 256 scans at 6 cm^{-1} resolution. The Mössbauer spectra of all samples were recorded at room temperature, using a $^{57}Co(Rh)$ source and a computer driven constant acceleration mode spectrometer. The velocity scale was calibrated using high purity natural iron foil. Isomer shifts were established with respect to the center of gravity of the room temperature iron Mössbauer spectrum.

2.2. Photoelectrochemical measurements

In order to determine electronic states within the investigated materials the following procedure was applied: the samples were ground in a mortar, suspended in acetonitrile and were placed dropwise on platinum foil. The foil was then dried in a flow of hot air. The so prepared working electrode was then placed in a cuvette together with a Ag/Ag$^+$ electrode and a platinum wire as reference and counter electrodes, respectively. 0.1 M $LiClO_4$ in acetonitrile was used as an electrolyte. A Perkin-Elmer Lambda 12 spectrophotometer (equipped with a 5 cm dia. integrating sphere), together with a BioLogic SP-150 potentiostat, was used to record spectral changes as a function of potential. The spectra of as prepared electrodes were used as references. The external potential was applied stepwise, starting at 0.0 V vs. the Ag/Ag$^+$ electrode with a step of -0.5 V kept for 25 minutes, until a potential of -2.5 V was reached. At each step, starting at the tenth minute, the reflectance spectrum was recorded. From these experiments a 900 nm wavelength was selected to monitor changes during the reduction of the materials.

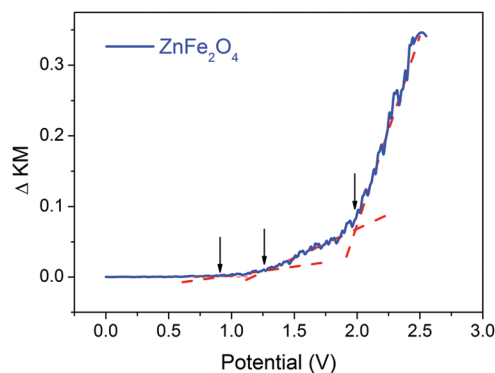Simplified DRS-SEC measurements (diffuse reflectance spectroscopy combined with spectroelectochemistry) were performed

Fig. 1 Typical results of the simplified DRS-SEC measurements used for determination of the potentials of the electronic states of the $ZnFe_2O_4$ spinel.

using the same experimental setup.[23–25] An external potential was applied to the working electrode starting from 0.0 V vs. the Ag/Ag⁺ electrode with a 50 mV s⁻¹ scanning speed until a potential of −2.5 V vs. Ag/Ag⁺ was reached. The reflectance changes were then transformed into the Kubelka–Munk function. The differential Kubelka–Munk plots were used to determine potentials of the electronic states within the band gap of the investigated spinel materials. As can be inferred from the plot in Fig. 1, the positions of electronic states correspond to the changes in the $\Delta KM = f(E)$ plot slope.

Photoelectrochemical measurements were carried out using a photoelectric spectrometer (Instytut Fotonowy). Measurements were performed in a three-electrode cell using a platinum wire and a Ag/AgCl electrode as counter and reference electrodes, respectively. A thin layer of material placed on ITO foil was used as a working electrode. The electrodes were placed in a cuvette with a quartz window filled with 0.1 mol dm⁻³ KNO_3 in deionized water as an electrolyte. The measurements were performed after saturation of the electrolyte with oxygen or argon (oxygen free conditions). Photocurrents were recorded upon irradiation within a range of 330–750 nm with a 20 nm step, and a potential range of −0.2 to 1.0 V vs. Ag/AgCl with a 50 mV step. The results are presented as IPCE (incident photon to current efficiency).

Work function (contact potential difference) measurements were performed with a Kelvin probe (McAllister KP6500). For each measurement 150 mg of the sample was pelletized (d = 10 mm) under 8 MPa pressure. The measurements were performed in a vacuum of 10⁻⁷ mbar at 150 °C after annealing the sample at 400 °C. This procedure was applied to assure the reproducibility of the measurements. A stainless steel electrode (d = 3 mm, ϕ = 4.1 eV) was used as a reference.

2.3.   Catalytic experiments

The temperature programmed oxidation method (TPO) was used to compare the activity of the prepared catalysts in soot combustion. A quartz fixed-bed reactor was heated (10 °C min⁻¹) from room temperature to 800 °C and a gas mixture of 5% O_2 in He at a 60 ml min⁻¹ flow rate was used during the tests. The reaction mixture, weighing 55 mg, was prepared by grinding a

catalyst sample with soot (Degussa—Printex80) in an 10 : 1 ratio. The mixture was ground for 10 minutes in the tight contact regime in an agate mortar. The soot combustion was monitored by a quadrupole mass spectrometer (SRS RGA200) following the lines for m/z = 44 (CO_2), 32 (O_2), 28 (CO), and 18 (H_2O). The conversion of soot was calculated by the integration of the QMS signal from CO_2.

3.   Results and discussion

3.1.   Characterization of spinel ferrites

3.1.1.   Thermal analysis of the $Co(OH)_2$–$Zn(OH)_2$–$Fe(OH)_3$ precursors. The thermal behavior of hydroxide precursors in non-isothermal conditions was studied in the range of 20–1000 °C. Thermogravimetric curves of the powders are presented in Fig. 2. The decrease in the weight of Co, Zn and Fe(III) hydroxides is due to their thermal decomposition and related to the loss of hygroscopic water and adsorbed gases. The total experimental weight loss (∼17%) is in good agreement with the theoretical values.

The derivative TG (DTG) curves for all samples indicate endothermic peaks corresponding to loss of water, including the dehydratation and dehydroxylation processes in the range 20–200 °C. Fig. 3 displays the positions of DTG peak temperatures for all precursor samples, which are in the range of 127 to 140 °C. The decomposition of precursors with the higher content of zinc occurs at the lowest temperatures, indicating that, by increasing the amount of zinc, the thermic effect decreases and shifts toward lower temperatures. It can be seen that the decomposition temperature peak for $CoFe_2O_4$ is 135 °C while for $ZnFe_2O_4$ it is 127 °C. This is in good agreement with ref. 26, because $Zn(OH)_2$ has a lower decomposition temperature (∼125 °C) in comparison with $Co(OH)_2$ (∼160 °C).

In DTA curves of the co-precipitated $Co_{1-x}Zn_xFe_2O_4$ powder precursors two thermic effects occur (the derivatograms of the most representative $CoFe_2O_4$ and $Zn_{0.5}Co_{0.5}Fe_2O_4$ powder precursors are shown in Fig. 4). The first one is a broad endothermic peak with a maximum around 150 °C which is associated with the thermal decomposition of the precipitated hydroxides due to the evaporation of the adsorbed water and then to the removal of constitutional water associated with the formation of metal oxides. The second exothermic peak is observed around 400 °C
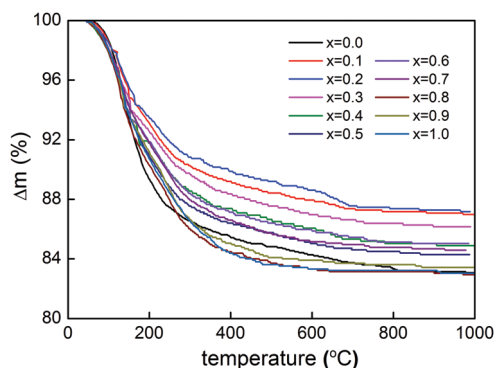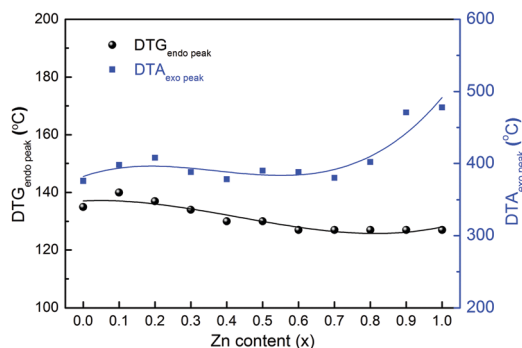

Fig. 2 TG curves for the $Co(OH)_2$–$Zn(OH)_2$–$Fe(OH)_3$ precursors.

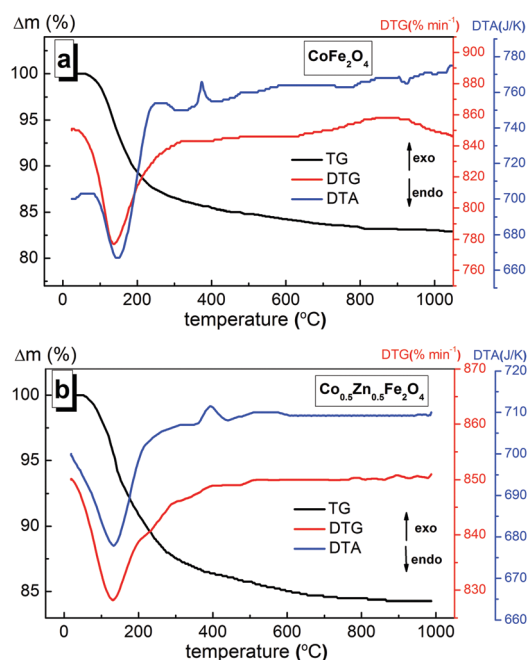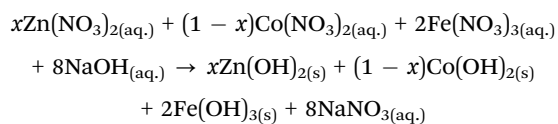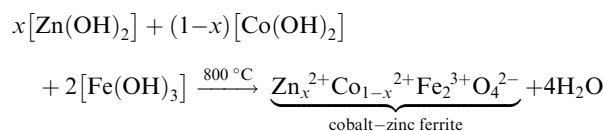**Fig. 3** DTG endo-peak and DTA exo-peak positions for the $Co_{1-x}Zn_xFe_2O_4$ system as a function of the Zn^{2+} content.

Fig. 4 TG, DTG and DTA curves of the most representative (a) $CoFe_2O_4$ and (b) $Zn_{0.5}Co_{0.5}Fe_2O_4$ powder precursors.

for samples with $x = 0.0$ to $x = 0.8$ and around 475 °C for samples with $x = 0.9$ and $x = 1.0$ (Fig. 3) and is attributed to the formation of the spinel structure. These data are in good agreement with the bibliographic data.[27,28] No other peaks were observed in DTG and DTA curves with the increase of the heating temperature up to 1000 °C which confirms that the samples are thermally stable and no phase transitions are observed.

A plausible mechanism of the precursor decomposition and spinel formation can be described in detail by the following steps. Firstly, metal hydroxide particles are formed due to interaction of metal cations (Co(II), Zn(II), Fe(III)) in the aqueous medium with sodium hydroxide solution (the co-precipitation step):

$$xZn(NO_3)_{2(aq.)} + (1 - x)Co(NO_3)_{2(aq.)} + 2Fe(NO_3)_{3(aq.)}$$
$$+ 8NaOH_{(aq.)} \rightarrow xZn(OH)_{2(s)} + (1 - x)Co(OH)_{2(s)}$$
$$+ 2Fe(OH)_{3(s)} + 8NaNO_{3(aq.)}$$

Thermal decomposition of the metal hydroxides leads to the formation of cobalt–zinc ferrite nanoparticles (the ferritization step):

$$x[Zn(OH)_2] + (1-x)[Co(OH)_2]$$
$$+ 2[Fe(OH)_3] \xrightarrow{800\ °C} \underbrace{Zn_x^{2+}Co_{1-x}^{2+}Fe_2^{3+}O_4^{2-}}_{cobalt-zinc\ ferrite} + 4H_2O$$

On the basis of the thermogravimetric studies (Fig. 2 and 3) the following synthesis conditions of the precursor powders were selected: 800 °C as the optimal temperature in order to obtain phases with good crystallinity and 2 hours as the optimal time for the synthesis process.

**3.1.2. FT-IR spectroscopy analysis of ferrite precursors.** In order to explain the transformation of the spinel precursors during the heating up to 800 °C infrared spectroscopy was applied. Fig. 5 shows the FTIR spectra of spinel precursors dried at 80 °C and spinel ferrites obtained at 800 °C. At higher wavenumbers of 3200–3600 cm^{-1} the FTIR spectra exhibit absorption bands which can be related to the –OH stretching vibrations of water (H–OH) and hydroxides (M(OH)$_n$).

The vibrational bands were associated with metal cations in the tetrahedral sites $(ZnO_4)^{6-}$, $(CoO_4)^{6-}$, and $(FeO_4)^{5-}$ and octahedral sites $(ZnO_6)^{10-}$, $(CoO_6)^{10-}$, and $(FeO_6)^{9-}$. The low frequency bands around 400 cm^{-1} are related to the tetrahedral groups, while high frequency bands around 600 cm^{-1} are related to the octahedral groups.

With increasing temperature the vibrational frequency bands related to the M–O bonds become more intense, while the vibrational frequency bands related to NO_3^-, OH^- and H_2O disappear.

3.1.3. Mössbauer spectral analysis and determination of the cationic distribution. Mössbauer spectra taken at room temperature are shown in Fig. 6. Up to $x = 0.5$ the spectra reveal magnetic ordering. For $x = 0.6$ traces of magnetic ordering are evidenced; for higher compositions only quadrupole doublets are observed. Other researchers reported similar data.[29–32]

The shape of Mössbauer spectra was described using the transmission integral method with CERN minimizing computer procedure MINUIT. Each subspectrum was characterized by the following hyperfine interaction parameters: magnetic field – B, isomer shift – IS, and quadruple splitting – QS. In the studied compounds Fe atoms reside in two sublattices: in the oxygen tetrahedral neighbourhood A sublattice and the octahedral oxygen coordination B sublattice. Because Fe atoms most strongly interact with ions from a counterpart sublattice, the largest influence on magnetic behaviour of Fe atoms in A sublattice comes from the 12 nearest metal ions from B sublattice and on Fe atoms in B sublattice – from 6 nearest metal ions from A sublattice. Gradual replacement of magnetic Co ions with non-magnetic Zn ions causes a strong reduction of the hyperfine magnetic field on Fe nuclei which are surrounded by Zn. Because Zn shows a strong preference to occupy the A sublattice[33–37] we assume that it influences only Fe atoms in the B sublattice.

$$\begin{array}{cc} A & B \\ (Co_{1-x-z}Zn_xFe_z) & (Fe_{2-z}Co_z)O_4 \end{array} \qquad (1)$$
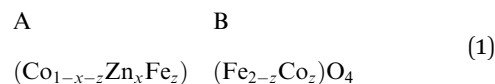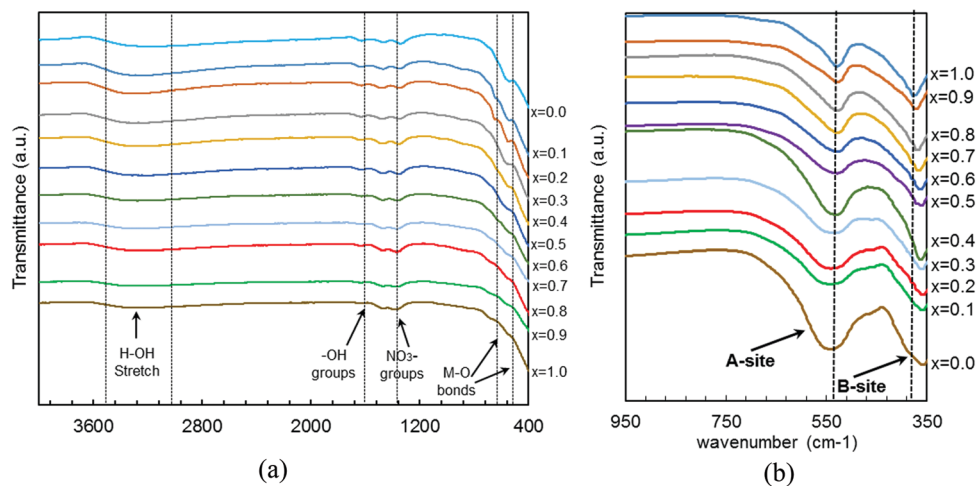
Fig. 5 FTIR spectra of spinel precursors (metal hydroxides) dried at 80 °C (a) and spinel ferrites obtained at 800 °C (b).

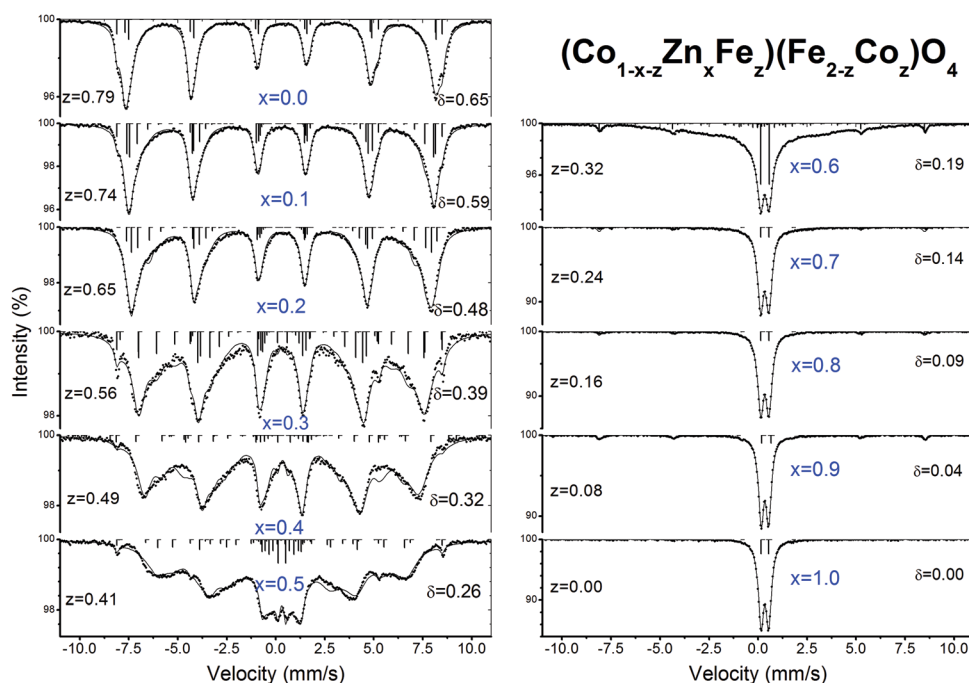Fig. 6 The ^{57}Fe Mössbauer transmission spectra taken at room temperature for $(Co_{1-x-z}Zn_xFe_z)_A[Fe_{2-z}Co_z]_BO_4$ (dots – experimental data, solid line – fitting result, $\delta = \dfrac{Fe_A^{3+}}{Fe_B^{3+}} = \dfrac{z}{2-z}$) (traces of hematite are evidenced for several compositions).

Fe atoms in the A-sublattice do not have Zn atoms as the nearest neighbours, hence it was assumed that in Mössbauer spectra only one Zeeman sextet corresponds to these Fe atoms. Fe atoms in the B sublattice have Zn atoms from the A sublattice as the nearest neighbours. The distribution of neighbours around Fe atoms from the B sublattice can be described by a binomial distribution

$$P(k) = \binom{n}{k} p^k (1-p)^{n-k} \quad n = 6, k = 0, 1, 2, 3, 4, 5, 6 \quad (2)$$

where $P(k)$ is the probability of finding k Zn atoms in the nearest neighbourhood of Fe atoms from the B sublattice,

and p corresponds to the probability of finding Zn atoms in the A sublattice, in our case $p = x$. We assumed that every single Zn ion coming into the Fe, located in the B sublattice, nearest neighbourhood causes the reduction of the hyperfine field by the same value, ΔB.

The distribution of Fe and Co atoms in the A and B sublattices is described by the partition parameter z (formula number 1) which was taken from XRD measurements.[22] This parameter is connected with the parameter δ $\left(\delta = \dfrac{Fe_A^{3+}}{Fe_B^{3+}} = \dfrac{z}{2-z}\right)$ which corresponds to the ratio of Fe atoms in the A and B sublattices and, in consequence, to the

ratio of the area of Zeeman spectra corresponding to the A and B sublattices.

Mössbauer spectra were fitted using the above procedure giving a good description of the spectra (Fig. 6). The final values of hyperfine interaction parameters obtained from fits are included in Table 1 and Fig. 7. The sextets attributed to B-octahedral sites come from different neighbourhoods containing different numbers of Zn atoms. The percentage contribution S of these sextets to the total spectrum is given in Table 1.

Thus the data obtained from Mössbauer spectroscopy confirmed the cationic distribution previously reported by our group in ref. 22. From the cationic distribution the difference in the Pauling electronegativities $\Delta\chi$ was calculated, which

showed the changes in the ionic bonds strength for the A- and B-sites. The difference in the electronegativity per cation for tetrahedral or octahedral sites was calculated using the following equations:[38]

$$\Delta\chi_A = \chi(O^{2-}) - \frac{\chi_A}{4} \qquad (3)$$

$$\Delta\chi_B = \chi(O^{2-}) - \frac{\chi_B}{6} \qquad (4)$$

where χ_A and χ_B are the Pauling electronegativities of the cations at the A- or B-sites respectively, and χ_O is the electronegativity of oxygen. The χ_A and χ_B values were estimated taking

Table 1 The values of Mössbauer hyperfine interaction parameters of $(Co_{1-x-z}Zn_xFe_z)(Fe_{2-z}Co_z)O_4$ (room temperature). (Sextet_A – tetrahedral site, Sextet_B – octahedral site (the number which follows indicates the number of Zn atoms in the nearest neighbourhood), IS – isomer shift, QS – quadrupole splitting, B – hyperfine field, Γ – line width, S – percentage contributions to the total spectrum, z – partition coefficient, data taken from ref. 22. Note that sextets with the lowest contribution were omitted)

Sample x (Zn)	Component	B [T] (±0.3)	IS [mm s^{-1}] (±0.02)	QS [mm s^{-1}] (±0.02)	Γ [mm s^{-1}] (±0.08)	S [%] (±2.0)	z (±0.1)
$x = 0.0$	Sextet A	49.20	0.23	−0.002	0.32	36.6	0.79
	Sextet B	48.70	0.35	−0.007	0.30	56.0	
$x = 0.1$	Sextet A	48.20	0.26	0.029	0.27	35.7	0.74
	Sextet B_0	48.93	0.32	−0.048	0.27	32.3	
	Sextet B_1	45.61	0.32	−0.047	0.27	21.5	
	Sextet B_2	42.29	0.32	−0.046	0.27	6.0	
	Sextet B_3	38.97	0.32	−0.045	0.27	0.9	
$x = 0.2$	Sextet A	47.58	0.27	0.014	0.26	32.5	0.65
	Sextet B_0	49.22	0.33	−0.021	0.30	17.7	
	Sextet B_1	45.60	0.33	−0.019	0.30	26.5	
	Sextet B_2	41.98	0.33	−0.017	0.30	16.6	
	Sextet B_3	38.36	0.33	−0.015	0.30	5.5	
$x = 0.3$	Sextet A	45.20	0.26	0.030	0.24	26.9	0.56
	Sextet B_0	50.90	0.34	−0.083	0.29	8.1	
	Sextet B_1	45.39	0.34	−0.046	0.29	20.9	
	Sextet B_2	39.88	0.34	0.010	0.29	22.4	
	Sextet B_3	34.37	0.34	0.027	0.29	12.8	
	Sextet B_4	28.86	0.34	0.063	0.29	4.1	
	Doublet A	—	0.34	0.250	0.16	0.8	
	Doublet B	—	0.34	0.250	0.16	0.3	
$x = 0.4$	Sextet A	43.12	0.27	0.011	0.21	23.7	0.49
	Sextet B_0	51.58	0.33	−0.033	0.27	3.4	
	Sextet B_1	44.90	0.33	−0.021	0.27	13.6	
	Sextet B_2	38.22	0.33	−0.009	0.27	22.7	
	Sextet B_3	31.54	0.33	0.002	0.27	20.2	
	Sextet B_4	24.86	0.33	0.014	0.27	10.1	
	Sextet B_5	18.18	0.33	0.026	0.27	2.7	
	Doublet A	—	0.35	0.260	0.20	2.1	
	Doublet B	—	0.35	0.260	0.20	0.7	
$x = 0.5$	Sextet A	39.10	0.28	−0.012	0.18	19.4	0.41
	Sextet B_0	50.39	0.22	−0.108	0.25	1.2	
	Sextet B_1	41.92	0.22	−0.098	0.25	7.1	
	Sextet B_2	33.45	0.22	−0.088	0.25	17.6	
	Sextet B_3	24.98	0.22	−0.078	0.25	23.5	
	Sextet B_4	16.51	0.22	−0.068	0.25	17.6	
	Sextet B_5	8.04	0.22	−0.058	0.25	7.1	
	Doublet A	—	0.31	0.190	0.16	3.2	
	Doublet B	—	0.31	0.190	0.16	0.8	
$x = 0.6$	Doublet A	—	0.35	0.220	0.25	26.0	0.32
	Doublet B	—	0.35	0.220	0.25	5.0	
$x = 0.7$	Doublet A	—	0.34	0.210	0.24	82.7	0.24
	Doublet B	—	0.34	0.210	0.22	11.3	
$x = 0.8$	Doublet A	—	0.34	0.210	0.22	87.4	0.16
	Doublet B	—	0.34	0.210	0.22	7.6	
$x = 0.9$	Doublet A	—	0.35	0.190	0.18	89.3	0.08
	Doublet B	—	0.35	0.190	0.18	3.7	
$x = 1.0$	Doublet B	—	0.35	0.200	0.18	100	0.00
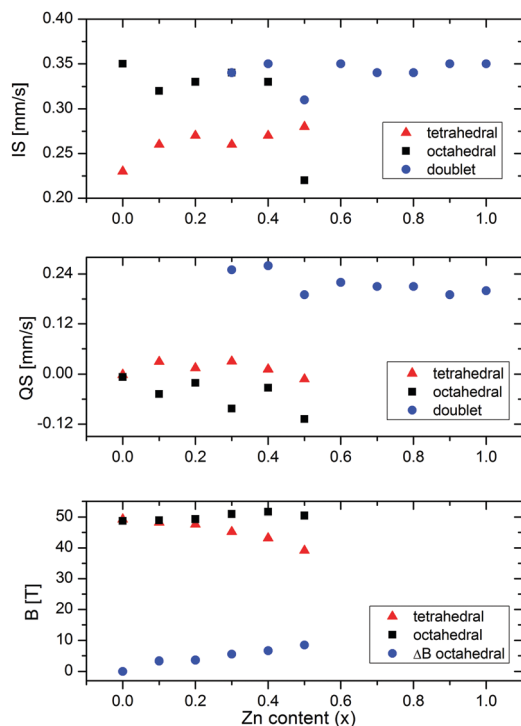
Fig. 7 Composition dependence of the hyperfine interaction parameters of $(Co_{1-x-z}Zn_xFe_z)(Fe_{2-z}Co_z)O_4$ obtained from Mössbauer spectroscopy.

into account the molar concentration of each cation at the A- or B-sites:

$$\chi_A = n(Co_A^{2+})\cdot\chi(Co^{2+}) + n(Zn_A^{2+})\cdot\chi(Zn^{2+}) + n(Fe_A^{3+})\cdot\chi(Fe^{3+})$$
(5)

$$\chi_B = \frac{n(Co_B^{2+})\cdot\chi(Co^{2+}) + n(Fe_B^{3+})\cdot\chi(Fe^{3+})}{2}$$
(6)

where $\chi(Co^{2+}) = 1.88$, $\chi(Zn^{2+}) = 1.65$, $\chi(Fe^{3+}) = 1.83$, and $\chi(O^{2-}) = 3.44$. The values of $\Delta\chi_A$ and $\Delta\chi_B$ are given in Table 2. The increasing $\Delta\chi_A$ and $\Delta\chi_B$ indicate decreasing bond strength in the tetrahedral and octahedral sites. This should influence the physicochemical properties and catalytic activity of the materials.

Table 2 Distances between magnetic ions (hopping length) in the A-sites (L_{A-A}), B-sites (L_{B-B}), and shared sites (L_{A-B}), and polaron radii (R_p) of $Co_{1-x}Zn_xFe_2O_4$ ferrites

x (Zn)	$\Delta\chi_A$	$\Delta\chi_B$	L_{A-A}	L_{B-B}	L_{A-B}	R_p
0	2.980	3.1317	2.953	3.617	3.463	0.530
0.1	2.985	3.1319	2.963	3.628	3.474	0.535
0.2	2.990	3.1323	2.966	3.633	3.478	0.537
0.3	2.994	3.1327	2.969	3.637	3.482	0.538
0.4	2.999	3.1330	2.970	3.638	3.483	0.539
0.5	3.004	3.1333	2.972	3.640	3.485	0.540
0.6	3.009	3.1337	2.974	3.643	3.487	0.541
0.7	3.013	3.1340	2.978	3.648	3.493	0.543
0.8	3.018	3.1343	2.977	3.647	3.491	0.543
0.9	3.023	3.1347	2.981	3.651	3.496	0.545
1	3.028	3.1350	2.984	3.654	3.499	0.546

The distance between the centers of adjacent ions (hopping length) in the A-sites (L_{A-A}), B-sites (L_{B-B}) and shared sites (L_{A-B}) can be evaluated using the following equations:[39]

$$L_{M_A-M_A} = a\frac{\sqrt{2}}{4}$$
(7)

$$L_{M_B-M_B} = a\frac{\sqrt{3}}{4}$$
(8)

$$L_{M_A-M_B} = a\frac{\sqrt{11}}{8}$$
(9)

The doping with larger Zn^{2+} results in an increase of the distance between the magnetic ions (Table 2). It is known[40] that in the spinel ferrites the charge carriers are localized in the d-shells of metal cations which leads to formation of polarons.[41] A polaron is a quasiparticle in a crystal consisting of an electron and a polarization cloud accompanying it. The formation of polarons leads to decreasing electron mobility in the crystal lattice. The values of polaron radii (R_p) were calculated using the following relation:

$$R_p = \frac{1}{2}\left[\frac{\pi}{6N}\right]^{1/3}$$
(10)

where N is the number of sites per unit volume ($N = 96/a^3$). The estimated values of the hopping lengths L_{A-A}, L_{B-B} and L_{A-B} and polaron radii are shown in Table 2. The values R_p are found to be smaller in comparison to interionic distances which could be due to the formation of small polarons. It was found that both hopping lengths and R_p increase with increasing Zn content. A higher energy is required for hopping from one cationic site to another which influences the catalytic activity of nanoferrites.

3.2. Photoelectrochemical properties and catalytic activity

In order to explain the semiconductor properties of the synthesized samples the electronic states for all the materials were determined and are presented in Fig. 8. Characteristic potentials of the conduction band bottoms are depicted as thicker bars. As a general tendency, with increasing Zn-doping the conduction band bottom potentials lower gradually. In accordance with
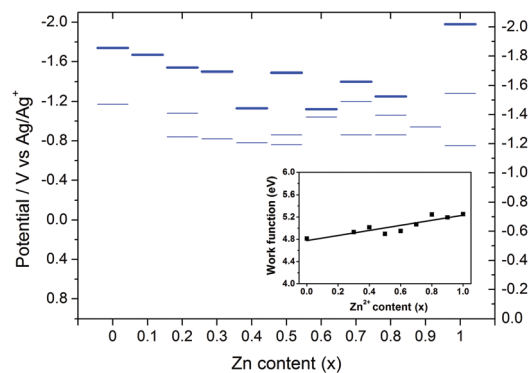

Fig. 8 Determined electronic states and work function (inset) for the $Co_{1-x}Zn_xFe_2O_4$ series as a function of zinc doping.

previously reported experiments for spinel materials the band gap is rather unaffected by the Zn content,[3,42] therefore, with increasing Zn-doping the valence band top also shifts towards higher potentials.

The results of the work function measurements are presented in Fig. 8 (inset). The work function varies from 4.82 eV to 5.25 eV for the samples with the lowest and highest zinc contents, respectively. Although the experimental work function values are somewhat scattered, the general correlation with the zinc content can be easily noticed. It is worth to underline that the observed trend is in line with the spectro-electrochemically determined levels of the conduction band bottom.

The photocurrent as a function of the incident light wavelength and the electrode potential was measured for selected materials. In Fig. 9 and 10 the results for two frontier spinels, namely $ZnFe_2O_4$ and $CoFe_2O_4$, are presented. All materials, despite their colors, are photocatalytically active only upon UV light irradiation. Interestingly, the influence of O_2 on the generated anodic photocurrents is different. In the case of $ZnFe_2O_4$ saturation of the electrolyte with oxygen leads to an increase of the IPCE values by a factor of almost 2, whereas for $CoFe_2O_4$ the effect is opposite (a decrease of the average IPCE by a factor of ca. 1.5). This indicates that the introduction of Zn^{2+} into the spinel structure modifies the ability of the materials to reduce O_2. At $CoFe_2O_4$ photoinduced reduction of dioxygen competes successfully with anodic photocurrent generation (observed as a decrease of photocurrent), while for $ZnFe_2O_4$ this process is negligible.

The soot oxidation measurements for the whole $Co_{1-x}Zn_x$-Fe_2O_4 series revealed substantial differences in catalytic activity. As seen in Fig. 11 the temperature of 50% soot conversion strongly depends on the spinel composition. The most active sample is the undoped $CoFe_2O_4$. The zinc content has a strong impact on the soot oxidation catalytic activity – substitution of cobalt with zinc cations led to a significant increase (by ca. 60 °C) of T_{50}. As shown before the efficiency of soot combustion catalyzed by transition metal oxides can be directly correlated with their work function values.[43,44] This tendency can be explained in terms of the electrodonor properties of the catalytic surface. The electron transfer from the catalyst to the O_2 molecules results in formation of reactive oxygen species,

Fig. 9 Examples ($ZnFe_2O_4$) of 3D plots of photocurrent vs. incident light wavelength and the electrode potential for oxygen free (a) and oxygen saturated (b) electrolyte.

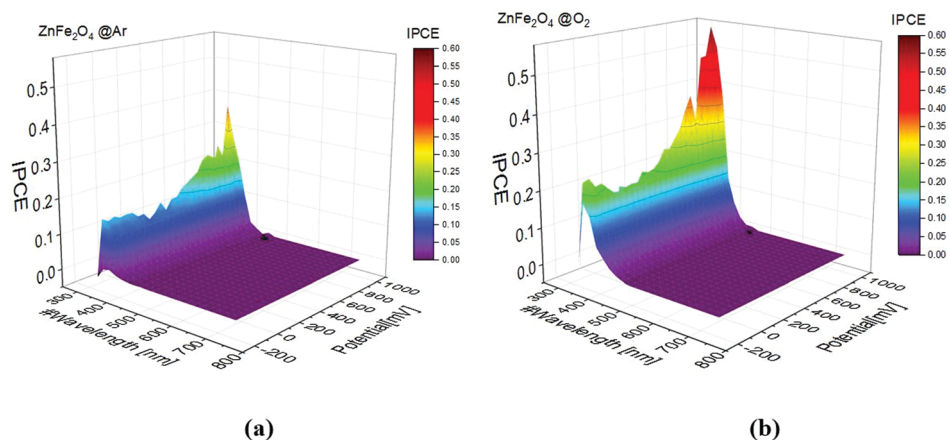**Fig. 10** Examples ($CoFe_2O_4$) of 3D plots of photocurrent vs. incident light wavelength and the electrode potential for oxygen free (a) and oxygen saturated (b) electrolyte.

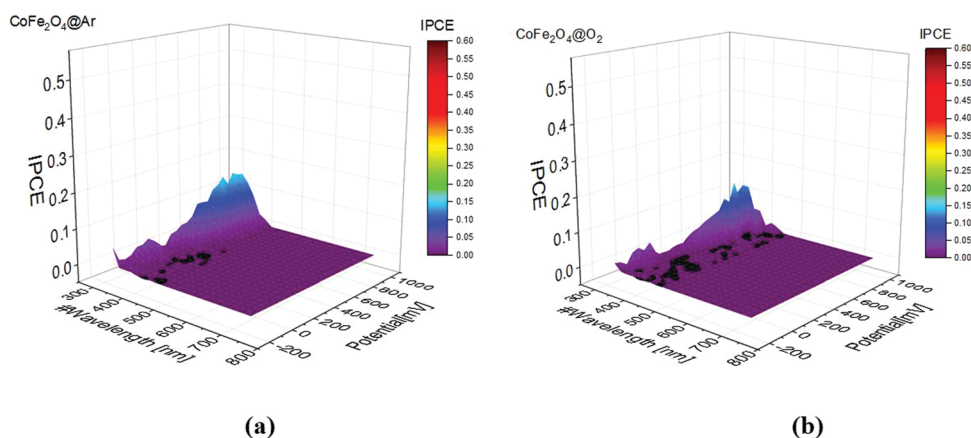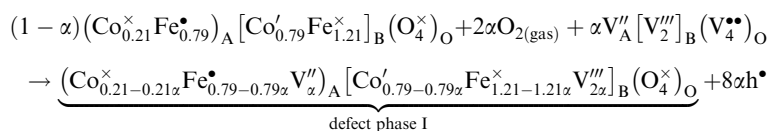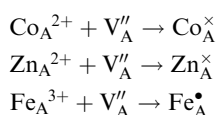such as O_2^- and even O_2^{2-}, responsible for the soot oxidation process.

In order to explain the higher activities observed for samples with higher cobalt content antistructure modeling[45–47] has been used. Antistructure modeling provides a resonance of spinel crystallochemical structure $(Me^{2+})_A[Me_2^{3+}]_B(O_4^{2-})_O$ with spinel antistructure $V_A''[V_2''']_B(V_4^{\bullet\bullet})_O$ and takes into account the presence of donor and acceptor active centers on the oxide
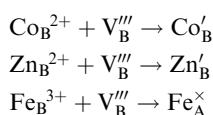
$$(1-\alpha)\left(Co_{0.21}^{\times}Fe_{0.79}^{\bullet}\right)_A\left[Co_{0.79}'Fe_{1.21}^{\times}\right]_B\left(O_4^{\times}\right)_O+2\alpha O_{2(gas)}+\alpha V_A''\left[V_2'''\right]_B\left(V_4^{\bullet\bullet}\right)_O$$

$$\rightarrow \underbrace{\left(Co_{0.21-0.21\alpha}^{\times}Fe_{0.79-0.79\alpha}^{\bullet}V_\alpha''\right)_A\left[Co_{0.79-0.79\alpha}'Fe_{1.21-1.21\alpha}^{\times}V_{2\alpha}'''\right]_B\left(O_4^{\times}\right)_O}_{\text{defect phase I}}+8\alpha h^{\bullet}$$

surfaces. The following equations explain the specific interactions between ions and vacancies:

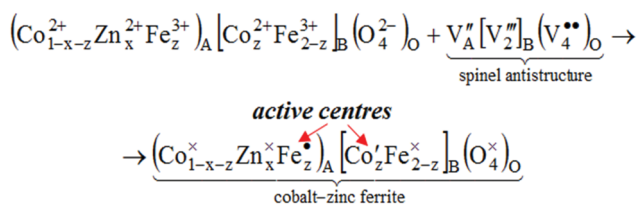| For A-sites:	For B-sites:
$Co_A^{2+}+V_A''\rightarrow Co_A^{\times}$	$Co_B^{2+}+V_B'''\rightarrow Co_B'$
$Zn_A^{2+}+V_A''\rightarrow Zn_A^{\times}$	$Zn_B^{2+}+V_B'''\rightarrow Zn_B'$
$Fe_A^{3+}+V_A''\rightarrow Fe_A^{\bullet}$	$Fe_B^{3+}+V_B'''\rightarrow Fe_A^{\times}$

where $\bullet$ – an excess positive charge; $''$ – a double excess negative charge; $'''$ – a triple excess negative charge; $\times$ – an effective zero charge; V – the cationic and anionic vacancies; A, B, O indices – tetrahedral, octahedral and anionic positions, respectively. Antistructure modeling was based on the Kröger–Vink notation and suggested that cobalt located in the B-sites acts as a surface active center for soot combustion due to an excess of negative charge:

$$\left(Co_{1-x-z}^{2+}Zn_x^{2+}Fe_z^{3+}\right)_A\left[Co_z^{2+}Fe_{2-z}^{3+}\right]_B\left(O_4^{2-}\right)_O+\underbrace{V_A''\left[V_2'''\right]_B\left(V_4^{\bullet\bullet}\right)_O}_{\text{spinel antistructure}}\rightarrow$$

$$\xrightarrow{\textbf{\textit{active centres}}}\underbrace{\left(Co_{1-x-z}^{\times}Zn_x^{\times}Fe_z^{\bullet}\right)_A\left[Co_z'Fe_{2-z}^{\times}\right]_B\left(O_4^{\times}\right)_O}_{\text{cobalt–zinc ferrite}}$$

The tetrahedral coordinated cobalt Co_A^{2+} does not act as an active center due to its effective zero charge. As we can see the concentration of octahedrally coordinated negatively charged donor active centers Co_B' and positively charged acceptor active centers $Fe_A^{\bullet}$ decreases with the increase of the Zn^{2+} content.
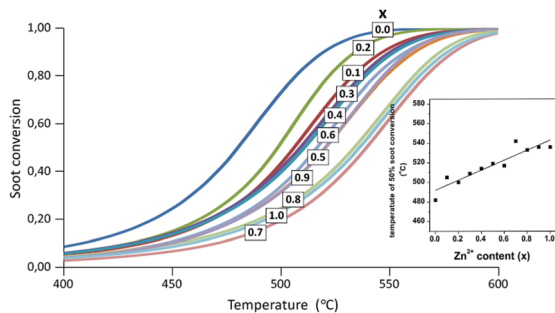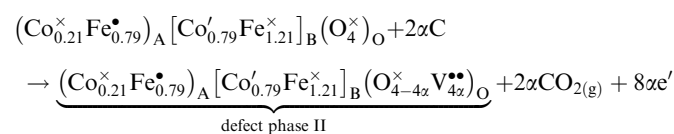

Fig. 11 Soot conversion as a function of temperature for the $Co_{1-x}Zn_x$-Fe_2O_4 series (inset: soot oxidation activity represented as the temperature of 50% soot conversion as a function of zinc content).
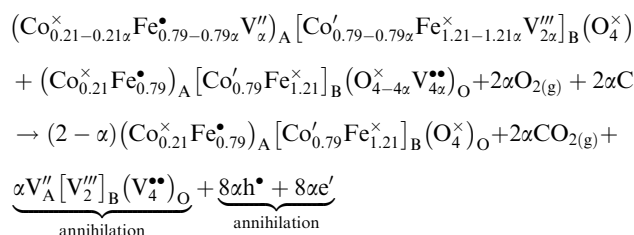
This is why the catalytic activity of $CoFe_2O_4$ in the soot combustion process is higher than for $ZnFe_2O_4$. The possible catalytic mechanism on the cobalt ferrite surface can be described by the following steps:

– the adsorption of $O_{2(g)}$ on the catalyst surface, and electron transfer from the catalyst to the O_2 molecules, which causes hole formation and vacancies in the tetrahedral and octahedral sublattices and formation of reactive oxygen species:

(See defect phase I equation above.)

– the soot particles react with surface lattice oxygen causing the formation of electrons e' and anionic vacancies $V_O^{\bullet\bullet}$:

$$2C+4O_O^{\times}\rightarrow 2CO_{2(g)}+4V_O^{\bullet\bullet}+8e'$$

$$\left(Co_{0.21}^{\times}Fe_{0.79}^{\bullet}\right)_A\left[Co_{0.79}'Fe_{1.21}^{\times}\right]_B\left(O_4^{\times}\right)_O+2\alpha C$$

$$\rightarrow\underbrace{\left(Co_{0.21}^{\times}Fe_{0.79}^{\bullet}\right)_A\left[Co_{0.79}'Fe_{1.21}^{\times}\right]_B\left(O_{4-4\alpha}^{\times}V_{4\alpha}^{\bullet\bullet}\right)_O}_{\text{defect phase II}}+2\alpha CO_{2(g)}+8\alpha e'$$

– reaction between the defect phases I and II which leads to annihilation of electron–hole pairs and the spinel antistructure:

$$\left(Co_{0.21-0.21\alpha}^{\times}Fe_{0.79-0.79\alpha}^{\bullet}V_\alpha''\right)_A\left[Co_{0.79-0.79\alpha}'Fe_{1.21-1.21\alpha}^{\times}V_{2\alpha}'''\right]_B\left(O_4^{\times}\right)$$

$$+\left(Co_{0.21}^{\times}Fe_{0.79}^{\bullet}\right)_A\left[Co_{0.79}'Fe_{1.21}^{\times}\right]_B\left(O_{4-4\alpha}^{\times}V_{4\alpha}^{\bullet\bullet}\right)_O+2\alpha O_{2(g)}+2\alpha C$$

$$\rightarrow(2-\alpha)\left(Co_{0.21}^{\times}Fe_{0.79}^{\bullet}\right)_A\left[Co_{0.79}'Fe_{1.21}^{\times}\right]_B\left(O_4^{\times}\right)_O+2\alpha CO_{2(g)}+$$

$$\underbrace{\alpha V_A''\left[V_2'''\right]_B\left(V_4^{\bullet\bullet}\right)_O}_{\text{annihilation}}+\underbrace{8\alpha h^{\bullet}+8\alpha e'}_{\text{annihilation}}$$

Summing up, the electronic properties (work function measurements, spectroelectrochemical characterization) indicate $CoFe_2O_4$ as the most efficient reductant in the studied series of spinels. As a consequence, this material offers the most efficient O_2 activation (reduction) *via* electron transfer. It implies straightforward consequences in the chemical (catalytic) reactivity. Indeed, the activity tests, both photocurrent generation and soot oxidation, show the highest activity of $CoFe_2O_4$. On the other hand, $ZnFe_2O_4$ is less active towards soot oxidation (poorer activation of oxygen), however, this material offers more efficient photoinduced charge separation (higher IPCE values compared to $CoFe_2O_4$).

The obtained results and concluded functional correlations provide a suitable platform for developing new materials for catalytic and photocatalytic applications. Although at this stage the studied mixed spinels do not compete with the best noble metal based systems (soot oxidation) or TiO_2-based photocatalysts (O_2 reduction) yet, the gathered knowledge may funnel future research towards rational design of more efficient catalysts.

4. Conclusions

The effect of Zn substitution on the structure–property relationship in Zn-doped cobalt ferrites ($Co_{1-x}Zn_xFe_2O_4$, where x ranges

from 0.0 to 1.0 with a step of 0.1) prepared by the co-precipitation method has been studied using thermal analysis, FTIR spectroscopy, Mössbauer spectroscopy, and diffuse reflectance spectroscopy combined with spectroelectochemistry and photoelectrochemical measurements. The FTIR analysis of precursors (Co(II), Zn(II) and Fe(III) hydroxides) and ferrites, obtained by the co-precipitation method, confirmed formation of the M–O bonds and spinel structure. The samples have been measured with ^{57}Fe Mössbauer spectroscopy at room temperature. The transmission integral fitting procedure of Mössbauer spectra was applied using a model of a binomial distribution of Zn atoms surrounding the B sublattice. It was found that the doping with larger Zn^{2+} ions in the $CoFe_2O_4$ lattice results in an increase of the distance between the magnetic ions. The values of polaron radii were calculated and are found to be smaller in comparison with interionic distances due to the formation of small polarons. All materials were photocatalytically active only upon UV light irradiation. Introduction of Zn^{2+} into the spinel structure modified the ability of the materials to reduce O_2: at $CoFe_2O_4$ photoinduced reduction of dioxygen competes successfully with anodic photocurrent generation (observed as a decrease of photocurrent), while for $ZnFe_2O_4$ this process was negligible. The activity tests (photocurrent generation and soot oxidation) showed the highest activity of $CoFe_2O_4$ which offered the most efficient O_2 activation (reduction) via electron transfer. The presence of Co^{2+} in Co–Zn ferrite catalysts significantly reduces the temperature window for catalytic soot combustion. The new antistructure modeling was proposed for explanation of the mechanism of catalytic processes: $CoFe_2O_4$ was more active in the soot oxidation reaction than zinc ferrite due to the presence of octahedrally coordinated negatively charged donor active centers Co'_B. The changes in concentration of donor active centers Co'_B and acceptor active centers $Fe^{\bullet}_A$ were explained. The current research demonstrated the deep relation between the cationic distribution and catalytic properties of Co–Zn ferrite nanoparticles.

Conflicts of interest

There are no conflicts of interest to declare.

Acknowledgements

References

1 Q. Zhao, Z. Yan, C. Chen and J. Chen, Spinels: Controlled Preparation, Oxygen Reduction/Evolution Reaction Application, and Beyond, *Chem. Rev.*, 2017, **117**, 10121–10211, DOI: 10.1021/acs.chemrev.7b00051.

2 T. Tatarchuk, M. Bououdina, J. J. Vijaya and J. L. Kennedy, Spinel Ferrite Nanoparticles: Synthesis, Crystal Structure, Properties, and Perspective Applications, in *Nanophysics, Nanomaterials, Interface Studies, and Applications. NANO 2016, Springer Proceedings in Physics*, ed. O. Fesenko and L. Yatsenko, Springer, Cham, 2017, vol. 195, pp. 305–325, DOI: 10.1007/978-3-319-56422-7_22.

3 T. R. Tatarchuk, N. D. Paliychuk, M. Bououdina, B. Al-Najar, M. Pacia, W. Macyk and A. Shyichuk, Effect of cobalt substitution on structural, elastic, magnetic and optical properties of zinc ferrite nanoparticles, *J. Alloys Compd.*, 2018, **731**, 1256–1266, DOI: 10.1016/j.jallcom.2017.10.103.

4 H. Hou, G. Xu, S. Tan and S. Xiang, A facile hydrothermal synthesis of nanoscale $CuFe_2O_4$ spinels with enhanced infrared radiation performance, *J. Alloys Compd.*, 2018, **735**, 2205–2211, DOI: 10.1016/j.jallcom.2017.11.370.

5 K. Pemartin, C. Solans, J. Alvarez-Quintana and M. Sanchez-Dominguez, Synthesis of Mn–Zn ferrite nanoparticles by the oil-in-water microemulsion reaction method, *Colloids Surf., A*, 2014, **451**, 161–171, DOI: 10.1016/j.colsurfa.2014.03.036.

6 K. M. Srinivasamurthy, J. V. Angadi, S. P. Kubrin, S. Matteppanavar, D. A. Sarychev, P. Mohan Kumar, H. W. Azale and B. Rudraswamy, Tuning of ferrimagnetic nature and hyperfine interaction of Ni^{2+} doped cobalt ferrite nanoparticles for power transformer applications, *Ceram. Int.*, 2018, **44**, 9194–9203, DOI: 10.1016/j.ceramint.2018.02.129.

7 K. Kombaiah, J. Judith Vijaya, L. J. Kennedy, M. Bououdina and B. Al-Najar, Conventional and microwave combustion synthesis of optomagnetic $CuFe_2O_4$ nanoparticles for hyperthermia studies, *J. Phys. Chem. Solids*, 2018, **115**, 162–171, DOI: 10.1016/j.jpcs.2017.12.024.

8 K. Kombaiah, J. J. Vijaya, L. J. Kennedy, M. Bououdina and B. Al Najar, Self heating efficiency of $CoFe_2O_4$ nanoparticles: a comparative investigation on the conventional and microwave combustion method, *J. Alloys Compd.*, 2018, **735**, 1536–1545, DOI: 10.1016/j.jallcom.2017.11.279.

9 A. H. Ashour, A. I. El-Batal, M. I. A. Abdel Maksoud, G. S. El-Sayyad, S. Labib, E. Abdeltwab and M. M. El-Okr, Antimicrobial activity of metal-substituted cobalt ferrite nanoparticles synthesized by sol–gel technique, *Particuology*, 2018, **40**, 141–151, DOI: 10.1016/j.partic.2017.12.001.

10 K. Kombaiah, J. J. Vijaya, L. J. Kennedy, M. Bououdina, R. J. Ramalingam and H. A. Al-Lohedan, Okra extract-assisted green synthesis of $CoFe_2O_4$ nanoparticles and their optical, magnetic, and antimicrobial properties, *Mater. Chem. Phys.*, 2018, **204**, 410–419, DOI: 10.1016/j.matchemphys.2017.10.077.

11 G. Barrera, M. Coisson, F. Celegato, S. Raghuvanshi, F. Mazaleyrat, S. N. Kane and P. Tiberto, Cation distribution effect on static and dynamic magnetic properties of $Co_{1-x}Zn_xFe_2O_4$ ferrite powders, *J. Magn. Magn. Mater.*, 2018, **456**, 372–380, DOI: 10.1016/j.jmmm.2018.02.072.

12 I. T. Cunha, I. F. Teixeira, A. S. Albuquerque, J. D. Ardisson, W. A. A. Macedo, H. S. Oliveira, J. C. Tristão, K. Sapag and R. M. Lago, Catalytic oxidation of aqueous sulfide in the presence of ferrites (MFe_2O_4, M = Fe, Cu, Co), *Catal. Today*, 2016, **259**, 222–227, DOI: 10.1016/j.cattod.2015.07.023.

13 S. Mobini, F. Meshkani and M. Rezaei, Surfactant-assisted hydrothermal synthesis of $CuCr_2O_4$ spinel catalyst and its application in CO oxidation process, *J. Environ. Chem. Eng.*, 2017, **5**, 4906–4916, DOI: 10.1016/j.jece.2017.09.027.

14 J. Hu, W. Zhao, R. Hu, G. Chang, C. Li and L. Wang, Catalytic activity of spinel oxides $MgCr_2O_4$ and $CoCr_2O_4$ for methane combustion, *Mater. Res. Bull.*, 2014, **57**, 268–273, DOI: 10.1016/j.materresbull.2014.06.001.

15 A. M. Banerjee, M. R. Pai, S. S. Meena, A. K. Tripathi and S. R. Bharadwaj, Catalytic activities of cobalt, nickel and copper ferrospinels for sulfuric acid decomposition: The high temperature step in the sulfur based thermochemical water splitting cycles, *Int. J. Hydrogen Energy*, 2011, **36**, 4768–4780, DOI: 10.1016/j.ijhydene.2011.01.073.

16 T. Tatarchuk, B. Al-Najar, M. Bououdina and M. A. A. Ahmed, Catalytic and Photocatalytic Properties of Oxide Spinels, in *Handbook of Ecomaterials*, ed. L. Martínez, O. Kharissova and B. Kharisov, Springer, Cham, 2019, DOI: 10.1007/978-3-319-48281-1_158-1.

17 D. Mukherjee and B. M. Reddy, Noble metal-free CeO_2-based mixed oxides for CO and soot oxidation, *Catal. Today*, 2018, **309**, 227–235, DOI: 10.1016/j.cattod.2017.06.017.

18 L. Tang, Z. Zhao, Y. Wei, J. Liu, Y. Peng and K. Li, Study on the coating of nano-particle and 3DOM $LaCoO_3$ perovskite-type complex oxide on cordierite monolith and the catalytic performances for soot oxidation: The effect of washcoat materials of alumina, silica and titania, *Catal. Today*, 2017, **297**, 131–142, DOI: 10.1016/j.cattod.2017.06.016.

19 T. Jakubek, W. Kaspera, P. Legutko, P. Stelmachowski and A. Kotarba, Surface versus bulk alkali promotion of cobalt-oxide catalyst in soot oxidation, *Catal. Commun.*, 2015, **71**, 37–41, DOI: 10.1016/j.catcom.2015.08.014.

20 H. Liu, X. Dai, K. Wang, Z. Yan and L. Qian, Highly efficient catalysts of $Mn_{1-x}Ag_xCo_2O_4$ spinel oxide for soot combustion, *Catal. Commun.*, 2017, **101**, 134–137, DOI: 10.1016/j.catcom.2017.08.007.

21 Z. Shang, M. Sun, S. Chang, X. Che, X. Cao, L. Wang, Y. Guo, W. Zhan, Y. Guo and G. Lu, Activity and stability of Co_3O_4-based catalysts for soot oxidation: The enhanced effect of Bi_2O_3 on activation and transfer of oxygen, *Appl. Catal., B*, 2017, **209**, 33–44, DOI: 10.1016/j.apcatb.2017.02.074.

22 T. Tatarchuk, M. Bououdina, N. Paliychuk, I. Yaremiy and V. Moklyak, Structural characterization and antistructure modeling of cobalt-substituted zinc ferrites, *J. Alloys Compd.*, 2017, **694**, 777–791, DOI: 10.1016/j.jallcom.2016.10.067.

23 E. Świętek, K. Pilarczyk, J. Derdzińska, K. Szaciłowski and W. Macyk, Redox characterization of semiconductors based on electrochemical measurements combined with UV-Vis diffuse reflectance spectroscopy, *Phys. Chem. Chem. Phys.*, 2013, **15**, 14256–14261, DOI: 10.1039/C3CP52129J.

24 M. Buchalska, M. Kobielusz, A. Matuszek, M. Pacia, S. Wojtyła and W. Macyk, On Oxygen Activation at Rutile- and Anatase-TiO_2, *ACS Catal.*, 2015, **5**, 7424–7431, DOI: 10.1021/acscatal.5b01562.

25 M. Kobielusz, K. Pilarczyk, E. Świętek, K. Szaciłowski and W. Macyk, Spectroelectrochemical analysis of TiO_2 electronic

states – Implications for the photocatalytic activity of anatase and rutile, *Catal. Today*, 2018, **309**, 35–42, DOI: 10.1016/j.cattod.2017.11.013.

26 W. M. Haynes, *CRC Handbook of chemistry and physics: A ready-reference book of chemical and physical data*, CRC Press, Boca Raton, 2009.

27 K. S. Ramakrishna, C. Srinivas, S. S. Meena, B. V. Tirupanyam, P. Bhatt, S. M. Yusuf, C. L. Prajapat, D. M. Potukuchi and D. L. Sastry, Investigation of cation distribution and magneto-crystalline anisotropy of $Ni_xCu_{0.1}Zn_{0.9-x}Fe_2O_4$ nanoferrites: Role of constant mole percent of Cu^{2+} dopant in place of Zn^{2+}, *Ceram. Int.*, 2017, **43**, 7984–7991, DOI: 10.1016/j.ceramint.2017.03.078.

28 S. B. Singh, C. Srinivas, B. V. Tirupanyam, C. L. Prajapat, M. R. Singh, S. S. Meena, P. Bhatt, S. M. Yusuf and D. L. Sastry, Structural, thermal and magnetic studies of $Mg_xZn_{1-x}Fe_2O_4$ nanoferrites: study of exchange interactions on magnetic anisotropy, *Ceram. Int.*, 2016, **42**, 19179–19186, DOI: 10.1016/j.ceramint.2016.09.081.

29 V. Mameli, A. Musinu, A. Ardu, G. Ennas, D. Peddis, D. Niznansky, C. Sangregorio, C. Innocenti, T. K. T. Nguyen and C. Cannas, Studying the effect of Zn-substitution on the magnetic and hyperthermic properties of cobalt ferrite nanoparticles, *Nanoscale*, 2016, **8**, 10124–10137, DOI: 10.1039/C6NR01303A.

30 D. Kotsikau, V. Pankov, E. Petrova, V. Natarov, D. Filimonov and K. Pokholok, Structural, magnetic and hyperfine characterization of $Zn_xFe_{3-x}O_4$ nanoparticles prepared by sol-gel approach via inorganic precursors, *J. Phys. Chem. Solids*, 2018, **114**, 64–70, DOI: 10.1016/j.jpcs.2017.11.004.

31 S. P. John and J. Mathew, Determination of ferromagnetic, superparamagnetic and paramagnetic components of magnetization and the effect of magnesium substitution on structural, magnetic and hyperfine properties of zinc ferrite nanoparticles, *J. Magn. Magn. Mater.*, 2019, **475**, 160–170, DOI: 10.1016/j.jmmm.2018.11.030.

32 S. Güner, A. Baykal, Md. Amir, H. Güngüneş, M. Geleri, H. Sözeri, E. S. Sagar and M. Sertkol, Synthesis and characterization of oleylamine capped $Mn_xFe_{1-x}Fe_2O_4$ nanocomposite: Magneto-optical properties, cation distribution and hyperfine interactions, *J. Alloys Compd.*, 2016, **688**, 675–686, DOI: 10.1016/j.jallcom.2016.07.033.

33 R. C. O'Handley, *Modern Magnetic Materials*, John Wiley & Sons, Inc, New York, 2000.

34 S. W. Lee and C. S. Kim, Mössbauer studies on the super-paramagnetic behavior of $CoFe_2O_4$ with a few nanometers, *J. Magn. Magn. Mater.*, 2006, **303**, e315–e317, DOI: 10.1016/j.jmmm.2006.01.042.

35 T. A. S. Ferreira, J. C. Waerenborgh, M. H. R. M. Mendonca, M. R. Nunes and F. M. Costa, Structural and morphological characterization of $FeCo_2O_4$ and $CoFe_2O_4$ spinels prepared by a coprecipitation method, *Solid State Sci.*, 2003, **5**, 383–392, DOI: 10.1016/S1293-2558(03)00011-6.

36 R. S. de Biasi and L. H. C. Cardoso, A simple model for the magnetocrystalline anisotropy in mixed ferrite nanoparticles, *Physica B*, 2012, **407**, 3893–3896, DOI: 10.1016/j.physb.2012.06.017.

37 A. Ghasemi, V. Sepelak, S. E. Shirsath, X. Liu and A. Morisako, Mössbauer spectroscopy and magnetic characteristics of $Zn_{1-x}Co_xFe_2O_4$ (x = 0–1) nanoparticles, *J. Appl. Phys.*, 2011, **109**, 07A512, DOI: 10.1063/1.3553777.

38 K. A. Mohammed, A. D. Al-Rawas and A. M. Gismelseed, *et al.*, Infrared and structural studies of $Mg_{1-x}Zn_xFe_2O_4$ ferrites, *Phys. B*, 2012, **407**, 795–804, DOI: 10.1016/j.physb. 2011.12.097.

39 M. D. Rahaman, T. Nusrat, R. Maleque and A. K. M. Akther Hossain, Investigation of structural, morphological and electromagnetic properties of $Mg_{0.25}Mn_{0.25}Zn_{0.5-x}Sr_xFe_2O_4$ ferrites, *J. Magn. Magn. Mater.*, 2018, **451**, 391–406, DOI: 10.1016/j.jmmm.2017.11.066.

40 N. H. Vasoya, V. K. Lakhani, P. U. Sharma, K. B. Modi, R. Kumar and H. H. Joshi, Study on the electrical and dielectric behaviour of Zn-substituted cobalt ferrialuminates, *J. Phys.: Condens. Matter*, 2006, **18**, 8063–8092, DOI: 10.1088/0953-8984/18/34/017.

41 A. J. Bosman and H. J. van Daal, Small-polaron versus band conduction in some transition-metal oxides, *Adv. Phys.*, 2006, **19**, 1–117, DOI: 10.1080/00018737000101071.

42 T. Tatarchuk, M. Bououdina, W. Macyk, O. Shyichuk, N. Paliychuk, I. Yaremiy, B. Al-Najar and M. Pacia, Structural, Optical, and Magnetic Properties of Zn-Doped $CoFe_2O_4$ Nanoparticles, *Nanoscale Res. Lett.*, 2017, **12**, 141–151, DOI: 10.1186/s11671-017-1899-x.

43 P. Legutko, W. Kaspera, P. Stelmachowski, Z. Sojka and A. Kotarba, Boosting the catalytic activity of magnetite in soot oxidation by surface alkali promotion, *Catal. Commun.*, 2014, **56**, 139–142, DOI: 10.1016/j.catcom.2014.07.020.

44 W. Kaspera, S. Zieliński and A. Kotarba, Alkali tungsten bronzes as soot oxidation catalysts: The key role of electrodonor properties of catalytic surface, *Catal. Commun.*, 2017, **98**, 76–80, DOI: 10.1016/j.catcom.2017.05.009.

45 S. N. Kane, S. Raghuvanshi, M. Satalkar, V. R. Reddy, U. P. Deshpande, T. R. Tatarchuk and F. Mazaleyrat, Synthesis, characterization and antistructure modeling of Ni nano ferrite, *AIP Conf. Proc.*, 2018, **1953**, 030089, DOI: 10.1063/1.5032424.

46 B. Rajesh Babu and T. Tatarchuk, Elastic properties and antistructural modeling for Nickel-Zinc Ferrite-Aluminates, *Mater. Chem. Phys.*, 2018, **207**, 534–541, DOI: 10.1016/j.matchemphys.2017.12.084.

47 T. Rajesh Kumar, P. Prabukanthan, G. Harichandran, J. Theerthagiri, T. Tatarchuk, T. Maiyalagan, G. Maia and M. Bououdina, Physicochemical and electrochemical properties of Gd3+-doped ZnSe thin films fabricated by single-step electrochemical deposition process, *J. Solid State Electrochem.*, 2018, **22**, 1197, DOI: 10.1007/s10008-017-3865-z.